JGR Solid Earth

RESEARCH ARTICLE
10.1029/2019JB018632

Special Section:
Ophiolites and Oceanic Lithosphere, with a focus on the Samail ophiolite in Oman

Timing of Magnetite Growth Associated With Peridotite-Hosted Carbonate Veins in the SE Samail Ophiolite, Wadi Fins, Oman

E. H. G. Cooperdock[1,2,3], D. F. Stockli[1], P. B. Kelemen[4], and J. C. de Obeso[4]

[1]Department of Geological Sciences, The University of Texas at Austin, Austin, TX, USA, [2]Department of Marine Chemistry and Geochemistry, Woods Hole Oceanographic Institution, Woods Hole, MA, USA, [3]Now at Department of Earth Sciences, University of Southern California, Los Angeles, CA, USA, [4]Department of Earth and Environmental Sciences, Columbia University, New York, NY, USA

Abstract Carbonate-altered peridotite are common in continental and oceanic settings and it has been suggested that peridotite-hosted carbonate represent a significant component of the carbon-cycle and provide an important link in the CO_2 dynamics between the atmosphere, hydrosphere, and lithosphere. The ability to constrain the timing of carbonate and accessory phase growth is key to interpreting the mechanisms that contribute to carbonate alteration, veining, and mineralization in ultramafic rocks. Here we examine a mantle section of the Samail ophiolite exposed in Wadi Fins in southeastern Oman where the peridotite is unconformably overlain by Late Cretaceous-Paleogene limestone and crosscut by an extensive network of carbonate veins and fracture-controlled alteration. Three previous $^{87}Sr/^{86}Sr$ measurements on carbonate vein material in the peridotite produce results consistent with vein formation involving Cretaceous to Eocene seawater (de Obeso & Kelemen, 2018, https://doi.org/10.1098/rsta.2018.0433). We employ (U-Th)/He chronometry to constrain the timing of hydrothermal magnetite in the calcite veins in the peridotite. Magnetite (U-Th)/He ages of crystal sizes ranging from 1 cm to 200 μm record Miocene growth at 15 ± 4 Ma, which may indicate (1) fluid–rock interaction and carbonate precipitation in the Miocene, or (2) magnetite (re)crystallization within pre-existing veins. Taken together with published Sr-isotope values, these results suggest that carbonate veining at Wadi Fins started as early as the Cretaceous, and continued in the Miocene associated with magnetite growth. The timing of hydrothermal magnetite growth is coeval with Neogene shortening and faulting in southern Oman, which points to a tectonic driver for vein (re)opening and fluid-rock alteration.

Key Points:
- The mantle section at Wadi Fins is altered by extensive carbonate veins with evidence for Fe mobility, forming magnetite in the veins
- Magnetite grew within carbonate veins at ca. 15 Ma, coincident with regional uplift
- (U-Th)/He dating of hydrothermal magnetite can be used for dating carbonate systems too old for ^{14}C or U-series techniques

Supporting Information:
- Supporting Information S1
- Table S1

Correspondence to:
E. H. G. Cooperdock,
cooperdo@usc.edu

Citation:
Cooperdock, E. H. G., Stockli, D. F., Kelemen, P. B., & de Obeso, J. C. (2020). Timing of magnetite growth associated with peridotite-hosted carbonate veins in the SE Samail ophiolite, Wadi fins, Oman. *Journal of Geophysical Research: Solid Earth*, *125*, e2019JB018632. https://doi.org/10.1029/2019JB018632

Received 4 SEP 2019
Accepted 29 MAR 2020
Accepted article online 6 APR 2020

1. Introduction

The Samail ophiolite in Oman and the United Arab Emirates provides unique access to an intact slice of oceanic crust and lithospheric mantle. However, due to the meta-stability of mantle peridotite minerals at Earth surface conditions, alteration effects associated deformation, fluid circulation, and low-temperature metamorphism are common within extensive mantle exposures. As such, the Samail ophiolite has also served as an important natural laboratory to study the chemical, physical, and biological effects of serpentinization and carbonation of mantle peridotite (e.g., Chavagnac, Ceuleneer, et al., 2013; Chavagnac, Monnin, et al., 2013; Clark & Fontes, 1990; Falk & Kelemen, 2015; Falk et al., 2016; Kelemen & Matter, 2008; Kelemen et al., 2011; Lacinska & Styles, 2012; Miller et al., 2016; Nasir et al., 2007; Neal & Stanger, 1983, 1984, 1985; Paukert et al., 2012; Stanger, 1985; Streit et al., 2012; Wilde et al., 2002).

Of particular interest are the mechanisms, timing, and durations of carbonate formation in altered peridotites. Carbonate minerals can either form by 1) growth or precipitation in fractures and veins, or 2) breakdown of peridotite or serpentinite minerals in the presence of CO_2-rich fluids, sourced from either seawater, magmatic fluids, atmosphere or fluid percolation (e.g., Klein & Garrido, 2011 and refs therein). These two styles of carbonate alteration in serpentinites have been observed at mid-ocean ridges, hyper-extended margins, and in exposed continental ophiolites, indicative of a prevalent process that occurs in a range of different geodynamic settings (e.g., Froitzheim & Rubatto, 1998; O'Neil & Barnes, 1971; Schroeder et al., 2002). Given the widespread nature of this process, it has been proposed that carbonate alteration and veining of ultramafic rocks plays an important role in the global C-cycle, affecting CO_2

concentrations in the atmosphere, and possibly impacting climate, ocean acidification, and C-recycling into the mantle (Jagoutz et al., 2016; Kelemen & Manning, 2015; Kerrick & Connolly, 1998; Reusch, 2011; Scambelluri et al., 2016; Schuiling & de Boer, 2010).

Quantifying when mineralization occurs in these systems is critical to understand the mechanisms and reaction rates of carbonate alteration within ultramafic rocks. The task of dating these systems comes with a set of challenges. Although carbonate can be directly dated by U-series (when sufficient U is present) or ^{14}C radiometric techniques (Dorale et al., 2004; Edwards et al., 2003; Ludwig et al., 2011), these are not applicable to the deep-time geologic record (i.e., >500 ky) where fossilized carbonate-altered peridotite systems are present in many settings. U–Pb and Pb–Pb geochronology techniques have been successfully applied to date older carbonate minerals (e.g., Goodfellow & Kylander-Clark, 2017; Hansman et al., 2018; Pisapia et al., 2017; Roberts & Walker, 2016), but can be hampered by the mobility of U and Pb, low U concentrations, thermal diffusion, and/or carbonate recrystallization (e.g., Jahn & Cuvellier, 1994; Smith et al., 1991). Hence, in many localities, when and/or how long carbonate alteration occurred has been interpreted based on relative timing or loose constraints.

Previous geochronology on peridotite-hosted carbonate in Oman has elucidated key feedbacks between the physical and geochemical processes that control peridotite alteration, both in terms of rates or durations of reactions, as well as timing of fluid–rock interactions relative to tectonic forces. For example, previous work on listvenite (carbonated peridotite) in the hanging wall of the basal thrust in Oman yielded a Rb-Sr age of 97 ± 26 Ma, which supports the interpretation that listvenite carbonation occurred during ophiolite obduction due to infiltration of CO_2-rich fluids derived from allochthonous continental margin sediments (Falk & Kelemen, 2015; Kelemen et al., 2011). Other work applied ^{14}C and U-series to more than 40 samples from peridotite hosted travertine deposits and carbonate veins from across the ophiolite, finding that vein deposition occurred in many locations over the past ~350 ky, especially the past ~50 ky, related to Quaternary groundwater cycling (Clark & Fontes, 1990; Kelemen et al., 2011; Kelemen & Matter, 2008; Mervine et al., 2014). Though a large number of peridotite-hosted carbonate veins formed in the Quaternary, some veins were too old for ^{14}C and U-series (Mervine et al., 2015), indicating a more ancient history that has yet to be constrained. The present study investigates the timing of alteration in a 'fossil' carbonate-veined peridotite system in Wadi Fins, Oman.

Wadi Fins is south of the main portion of the Samail ophiolite where samples for the aforementioned studies were collected (Figure 1). The peridotite at Wadi Fins is exposed in a small erosional window at the bottom of a wash (wadi) beneath limestone cliffs in the Tiwi-Sur area of Oman (Figure 1). Although, the carbonate veining within the serpentinized peridotite at Wadi Fins is similar to other localities in Oman, there are several distinct features summarized by de Obeso and Kelemen (2018, 2020) that make it unique. In particular, the high density of calcite veins in the peridotite below the unconformity with limestone. The chemical origin of the veins was investigated by de Obeso and Kelemen (2018), who concluded that the veins formed with fluids in equilibrium with the overlying limestone at high water-rock ratios (>1000) and at low temperatures (25–60 °C). The presence of calcite as the dominant carbonate mineral, and similar $\delta^{13}C$, $\delta^{18}O$, and $^{87}Sr/^{86}Sr$ signatures are further evidence for a genetic relationship with the overlying limestone units, which were deposited from Late Cretaceous to Paleogene (de Obeso & Kelemen, 2018; Schlüter et al., 2008). Here we use (U-Th)/He chronometry to further constrain when the system was active as recorded by hydrothermal magnetite growth within the calcite veins at Wadi Fins. These results, in addition to geochemical and geologic interpretations presented in de Obeso and Kelemen (2018, 2020), provide new insights into the history of vein opening or re-opening and mineralization.

1.1. Geologic Context

Wadi Fins is located in southeastern Oman near the town of Fins (Tiwi-Sur area) (Figure 1(a)) in an area where autochthonous Cretaceous to Tertiary sedimentary units were deposited on top of harzburgite and minor dunite from the Samail Nappe. Exposures of the ophiolite are limited to deeply incised canyons, such as at Wadi Fins (Figure 1(b)) (Al-Khirbash, 2015, 2016; Robertson, 1987; Wyns et al., 1992). Present day Wadi Fins has limestone cliffs atop an erosional unconformity with serpentinized sub-oceanic mantle harzburgite cropping out on the wadi floor (Figure 1(c)). The ultramafic rocks at Wadi Fins represent serpentinized harzburgite of the mantle section of the Samail ophiolite, obducted onto the Arabian margin in the Late Cretaceous (Hacker, 1994; Jacobs et al., 2015; Rioux et al., 2012, 2013; Searle & Cox, 1999, 2002). An

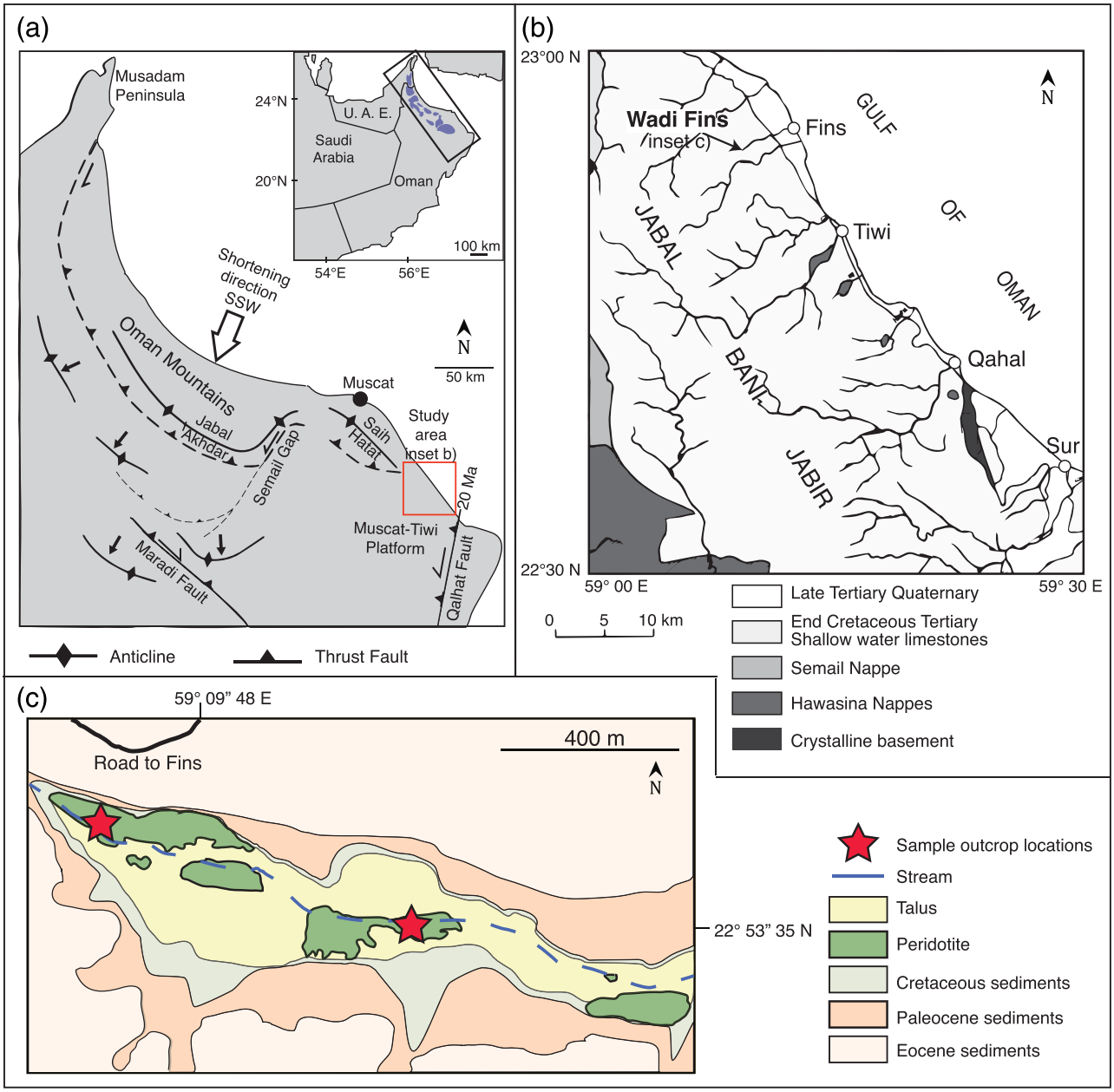

Figure 1. a) Map of Oman after Hansman et al., 2017 showing major structures related to post-obduction shortening. b) Geologic map of the region surrounding Wadi Fins after Wyns et al., 1992. The area is predominately covered by Late Cretaceous to Tertiary limestones with Samail and Hawasina Nappe lithologies exposed near faults or canyon floors. c) Geologic map of Wadi Fins after de Obeso & Kelemen, 2018 showing peridotite exposures (green) and sample locations as stars.

erosional contact and laterite deposits directly on the oceanic mantle section in this area indicates that it was subaerially exposed during the Early Maastrichtian (Al Khirbash, 2015, 2016; Alsharon & Nasir, 1996; Nolan et al., 1990; Skelton et al., 1990). Subsidence and carbonate deposition in the Late Maastrichtian buried the mantle rocks at Wadi Fins below 1–1.5 km of shallow marine limestones, which culminated around the Eocene times based on field relationships (Fournier et al., 2006; Robertson & Searle, 1990; Schlüter et al., 2008; Wyns et al., 1992).

The peridotite section within Wadi Fins is pervasively altered and cut by carbonate veins with reaction zones between carbonate and serpentine indicating fluid–rock interaction during vein development. Wadi Fins has several distinct features compared to other altered peridotite localities within Oman worth noting: 1)

Outcrop exposures are sub-parallel to, and 0–30 m beneath, a Late Cretaceous unconformity, overlain by minor fluvial conglomerates and extensive Late Cretaceous to Eocene limestones. 2) Outcrops are cut by "clastic dikes" with angular clasts of limestone and altered peridotite in a micritic limestone matrix, that extend 10 to 15 m below the unconformity, but are absent from the overlying limestone. 3) Extreme redox zonation is developed within the altered peridotite. 4) Veins in peridotite are composed almost exclusively of calcite, unlike elsewhere where veins in peridotite far from alkaline springs are dominantly composed of magnesite and dolomite (e.g., Kelemen et al., 2011; Kelemen & Matter, 2008). 5) There is an unusually high abundance of veins (5–10 volume %, compared to ~1% average in outcrops elsewhere) over tens of thousands of square meters in the peridotite below the unconformity, whereas veins are rare in the limestone above the unconformity.

Cross-cutting relationships show that carbonate veining post-dates some serpentinization; however, chrysotile and lizardite are present in the center of some veins. Within 20 m of the unconformity, many veins are flanked by distinctive, concentric alteration zones of Fe-poor and oxidized-Fe-rich serpentinites, though carbonate veins cross cut these zones as well (de Obeso & Kelemen, 2020). Clumped isotope data constrain carbonate vein formation temperatures between 25–60 °C (de Obeso & Kelemen, 2018). Carbonate mineralogy, $\delta^{13}C$, $\delta^{18}O$, and $^{87}Sr/^{86}Sr$ compositions of the carbonate veins are broadly consistent with deposition by fluids in equilibrium with the overlying limestone and the two out of three $^{87}Sr/^{86}Sr$ measurements match that of Cretaceous seawater (de Obeso & Kelemen, 2018), which constrains the timing of carbonate veining to the Maastrichtian at the earliest.

The timing of uplift that now exposes Wadi Fins is locally bracketed by stratigraphic relationships, but has not been directly dated (described in Fournier et al., 2006; Würsten et al., 1991; Wyns et al., 1992). In addition to the Late Cretaceous uplift and subsidence that formed the unconformity, Wyns and others (1992) argue that the area around Fins experienced Eocene extension based on continued subsidence and deposition of sedimentary units, which transitioned to Miocene compression as evidenced by deformation of Miocene units and the cessation of deposition. More recent Pliocene to Quaternary deformation is also documented along the Sur coastal plain with faults cutting alluvium and uplifted marine terraces (Kusky et al., 2005; Mattern & Scharf, 2018; Moraetis et al., 2019; Wyns et al., 1992).

To the north of Wadi Fins, uplift of the Oman Mountains has been investigated by low-temperature thermochronology. Multiple mechanisms have been invoked to explain the Cenozoic exhumation and uplift in the Central Oman Mountains, including compression related to far-field stresses of the Zagros collision (principally expressed in northern Oman) (Al-Lazki et al., 2002; Mann et al., 1990; Mouthereau et al., 2012; Robertson & Searle, 1990) or a slowdown of Makran subduction to the east affecting central Oman (Hansmann et al., 2017). Low-temperature thermochronometric data are broadly consistent with post-obduction cooling below 100 °C regionally by ~40–30 Ma based on apatite fission track and (U-Th)/He data (Grobe et al., 2019; Hansman et al., 2017; Poupeau et al., 1998; Saddiqi et al., 2006; Würsten et al., 1991). For the purposes of this study, the timing of deformational events and regional cooling history are important context for interpreting the significance of the magnetite (U-Th)/He data.

1.2. Sample Description

Magnetite samples were retrieved from two sample locations (~1 km apart within the canyon) distinguished by different alteration zones within the peridotite. The first sampling location (Figures 1(c), 2(a)-(c)), situated within 10 m of the limestone contact, displays unique green and red concentric alteration zones of fracture-bound serpentinite blocks (Figure 2(a)). These zoned blocks are 10's of cm across and bound on all sides by carbonate veins. Each block exhibits three distinct concentric alteration zones: a dark-green, partially serpentinized peridotite core, a light-green fully serpentinized rim, and a red fully oxidized serpentinized outer rim (denoted as 1, 2 and 3 in Figure 2(b)). Outside of this red-green zonation, calcite veins wrap and cross-cut the blocks of the serpentinite. Some veins also contain serpentine. In this outcrop, oxidized conditions are recorded by the presence of hematite and goethite in the red zones. Magnetite, distinguished by its major chemistry and magnetic character, is also present and found in the calcite veins (Figure 2c). Concentric zoning around some calcite veins suggests coeval oxidation and vein formation, while other veins cut the zoning and may postdate it. The relationship between magnetite growth and different vein generations is not straightforward to ascertain, as it was found in multiple vein types and orientations in both outcrop locations.

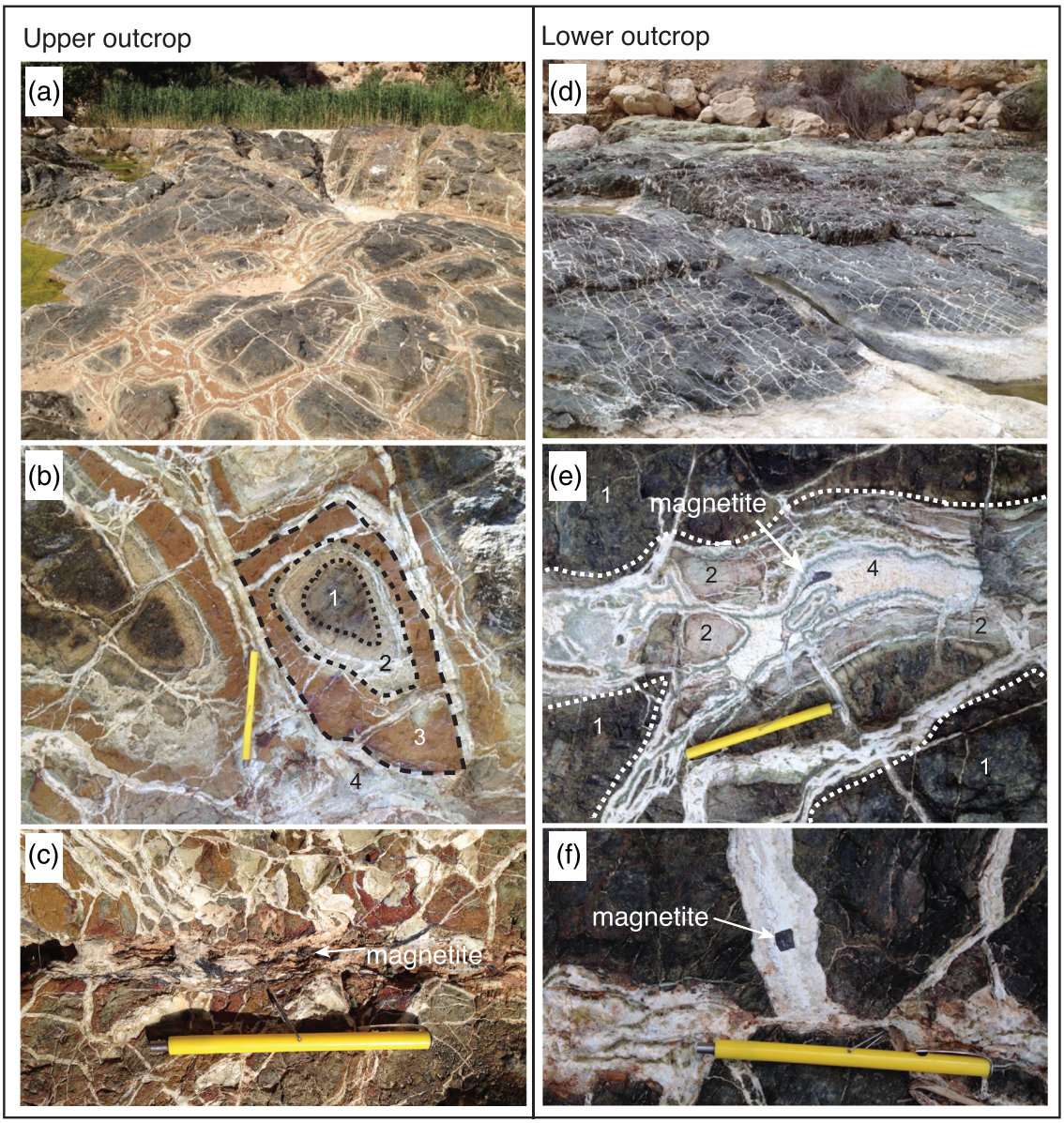

Figure 2. Outcrop photos showing calcite vein and alteration textures in the Wadi Fins serpentinized harzburgites. (a-c) Upper canyon outcrop, (d-f) lower canyon outcrop. a) Outcrop view ~10 m below the unconformity with red-green concentric zonation. b) Close up showing concentric zonation with dark green core (1), light green inner alteration rim (2), and red oxidized outer alteration rim (3). Multiple generations of carbonate veins cross cut the serpentinite (4). c) Example of sub-anhedral magnetite growth within a calcite vein. d) Lower canyon outcrop with checkerboard pattern of calcite veins. e) Close of up alteration zone in the lower outcrop showing dark green serpentinite (1), light green alteration near the calcite vein (2), and late stage calcite vein with green serpentine (4). f) Close up of lower outcrop vein network showing large, euhedral magnetite grain in the center of a vein. Note magnetite can form as euhedral crystals (f) or aggregates (c).

The second sample locality is ~1 km downstream and tens of meters below the limestone contact (Figures 1c, 2d-f). Here the outcrop is dominated by dark-green, partially serpentinized peridotite, similar to the least oxidized cores in the first outcrop, though more thoroughly serpentinized, with only narrow (<10 cm) light-green fully serpentinized reaction zones at the interface with calcite veins (denoted as 1 and 2 in Figure 2e). Extensive calcite veins are micrometers to multiple centimeters wide and laterally continuous for up to several meters, crosscutting serpentinite in a "checkerboard" pattern on the canyon floor (Figure 2d). Notably, this section does not have oxidized red alteration zones, as in the upper outcrop area. This area is similarly bound by calcite veins that in some cases host mm-size magnetite (Figures 2f). In

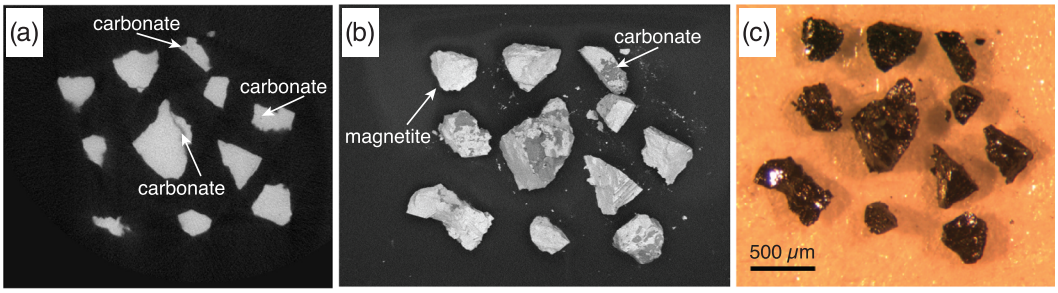

Figure 3. Magnetite grain images that show the co-genetic growth between magnetite and carbonate. a) X-ray computed tomography image (single data slice) that shows magnetite (bright gray) with carbonate (dark gray) inclusions and fractures. b) BSE image of magnetite grains with carbonate visible on the surface (darker gray material). c) Optical microscope image of the same magnetite grains, where the attached and intergrown carbonate is not visible on the opaque mineral surface. This illustrates the importance of CT and/or SEM screening of opaque phases for foreign material.

several locations, carbonate veins are accompanied by late-stage chrysotile and lizardite near the center of the veins (de Obeso & Kelemen, 2018) (Figure 2e).

Throughout both outcrops, magnetite is notably rare and when present very small (< 50 μm) in the serpentinite, suggesting that most of the Fe is hosted in other phases (like serpentine, see de Obeso & Kelemen, 2018, 2020). However, magnetite is observed as large, mm- to cm-size, euhedral crystals in the calcite veins or as sub-to-anhedral aggregates of sub-mm crystal trails along the interiors of calcite veins (Figure 2). Very low Fe concentrations in the calcite (<1 wt% Fe) require that Fe was scavenged elsewhere to form magnetite, most likely from the serpentinite hosting the veins (9 wt% Fe) (concentrations from de Obeso & Kelemen, 2018). These observations, as well as the presence of carbonate inclusions within magnetite crystals (Figure 3), support the interpretation that the magnetite crystals (or possibly an Fe-oxide precursor) grew concurrently with calcite precipitation.

Representative magnetite grains collected from the two sample locations are shown in Figure 4. One magnetite sample (15OM21, IGSN IEEHG001) was recovered from within a calcite vein adjacent to the red-green alteration zone in the upper outcrop near the limestone contact (Figure 2a). Additional magnetite crystals 15OM25B (IGSN IEEHG004), 15OM24bg (IGSN IEEHG002), and 15OM24g2 (IGSN IEEHG003) were plucked from calcite veins at the lower outcrop (Figures 4b-d). Other samples from the same locations were screened for magnetite He dating, but were not analyzed either due to their small magnetite grain size (<60 μm) or pervasive carbonate inclusions within the magnetite revealed by micro-CT scanning (as in Figure 3).

2. Methods

2.1. Sample Preparation

Magnetite grains were separated from carbonate vein material with mortar and pestle and subsequently removed by hand magnet. Sampled magnetite consisted of mm- to cm-size euhedral grains, that were hand crushed to ≥100 micron-size fragments, or smaller sub-mm anhedral grains making up magnetite clusters. Prior to (U-Th)/He analysis, magnetite grains were subjected to a multi-step screening and preparation process, including: 1) X-Ray Computed Tomography (CT) scanning, 2) the removal of the outer grain rims by air abrasion, and 3) semi quantitative determination of major element chemistry by scanning electron microscope (SEM-EDS).

Separated grains and fragments were picked using an optical microscope (up to 180x) onto double-sided sticky tape mounted plastic push pins for High-Resolution X-Ray CT scanning at the University of Texas at Austin's NSF-Multi User Facility (e.g., Cooperdock et al., 2019). The X-Ray CT screening is critical step to reveal the presence of inclusions or internal fractures that would complicate He diffusion systematics and lead to erroneous He age results (e.g., Cooperdock & Stockli, 2016). All analyzed grains were CT scanned at a 3–5-μm voxel spatial resolution and only grains without discernable inclusions or fractures were used for (U-Th)/He dating (see supporting information for settings).

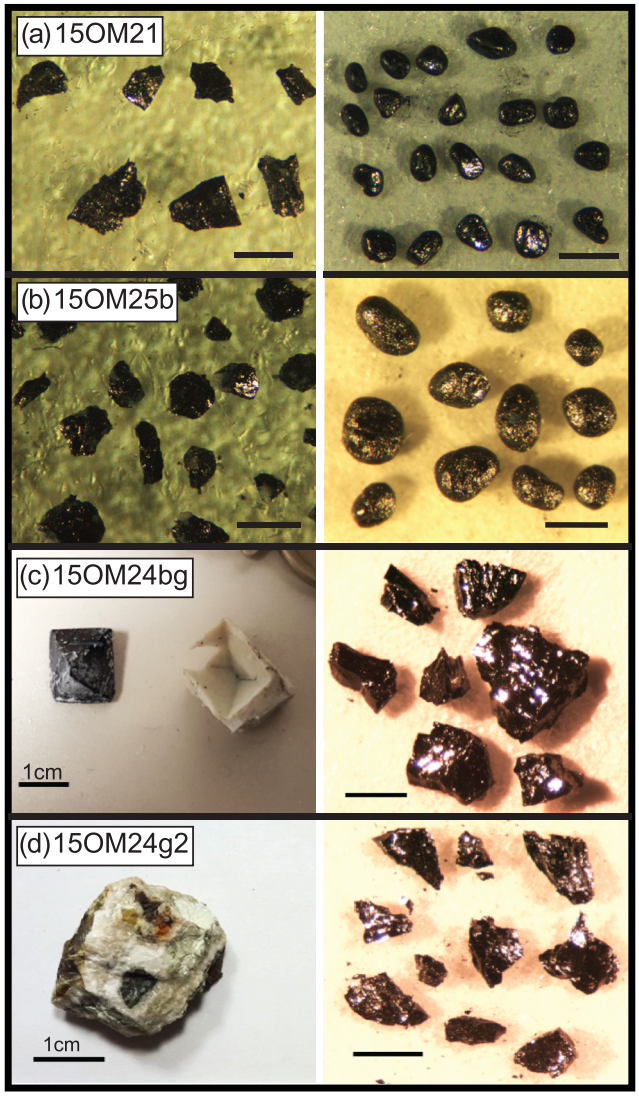

Figure 4. Representative sample separates before and after treatment to remove the outer grain boundaries. Scale bars are 500 μm unless otherwise noted. a) Population of anhedral magnetite crystals from the upper outcrop (left) and the same population of grains rounded after air abrasion (right). b) Anhedral magnetite crystals from the lower canyon outcrop (left) and representative grains after air abrasion (right). c) Large euhedral magnetite crystal (left) and internal fragments (right) from lower outcrop. d) Black magnetite grain (euhedral) surrounded by white calcite (left) from the lower outcrop and the same magnetite after crushing (right).

Due to low parent nuclide concentrations, magnetite is highly susceptible to U, Th or Sm contamination from attached matrix material or excess He due to implantation from neighboring phases (Blackburn et al., 2007; Cooperdock & Stockli, 2016). Since alpha particles (He nuclei) can travel ~16 μm in magnetite and be implanted from U- and Th-bearing neighboring phases, the outer ~20 μm of magnetite grains was removed prior to He analysis (e.g., Blackburn et al., 2007; Cooperdock & Stockli, 2016; Ketcham et al., 2011). Two preparation procedures were employed to remove these outer grain boundary domains. Large, mm- or cm-sized single grains (15OM24g2, 15OM24bg) were crushed with a mortar and pestle and internal fragments were selected under an optical microscope. Fragments were determined to be internal based on shiny luster, visually fractured surfaces and the lack of visible grain boundaries or attached matrix. Grains less than mm-size (15OM21, 15OM25B) were air abraded at 6 psi for ~4 hours following procedures described in Blackburn et al. (2007) and Cooperdock and Stockli (2016) (Figure 4).

Cooperdock and Stockli (2016) demonstrated that magnetite trace elements can be a useful complement to (U-Th)/He dating to differentiate between multiple growth episodes or grain populations, as hydrothermal magnetite can incorporate significant amounts of minor elements (e.g., Nadoll et al., 2014). For this purpose, semi-quantitative compositional data was collected on the surface of the same magnetite grains and fragments to be analyzed for (U-Th)/He using a Philips/FEI XL30 Environmental Scanning Electron Microscope (ESEM) with an X-ray energy dispersive spectroscopy (EDS) attachment at The University of Texas at Austin.

2.2. (U-Th)/He Measurements

All (U-Th)/He analyses were completed at the UTChron facility at The University of Texas at Austin. Individual sample aliquots, consisting of 1–8 abraded grains or internal fragments from a single grain, were loaded into platinum packets for in-vacuo laser He degassing. Only grains of similar size and composition (as determined by EDS) were combined into multi-grain aliquots. All aliquots were weighed on a microbalance with a < 1 μg precision prior to analysis. Masses are reported to the nearest μg. Individual aliquots were heated with a DiodeLaser using a pyrometer calibrated to a temperature of ~900 °C and ^{4}He concentrations were measured in two ways. Samples 15OM21 and 15OM25 were degassed using a Thermo HelixSFT™ magnetic-sector noble gas mass spectrometer, and samples 15OM24bg and 15OM24g2 were run on a Blazers Prisma quadrupole mass spectrometer. Blanks were run between each unknown to monitor and quantify the procedural baseline during analytical runs. Aliquots were reheated until ^{4}He gas yields dropped <1% total gas, or < 2x procedural blank concentrations. Total ^{4}He concentrations (ncc) were blank-corrected and determined against a manometrically-calibrated ^{4}He standard of known concentration.

After degassing, magnetite grains and fragments were removed from the platinum packets and dissolved following a two-step HF-HNO_3 and HCl dissolution technique and measured on a Thermo Element2 HR-ICP-MS following the procedure outlined in Cooperdock and Stockli (2016). U-Th-Sm concentrations were calculated using isotope dilution with a mixed spike calibrated against a 1 ppb U-Th-Sm gravimetric standard solution and blank-corrected using the average of multiple procedural blanks.

Final (U-Th)/He ages were calculated using blank corrected U, Th, Sm and He measurements for each aliquot. Reported concentrations were determined using the weighed mass of each aliquot. The reported error for individual (U-Th)/He ages represents a propagated analytical error for each measurement, plus the

standard deviation of the blanks and standards from each analytical run. A detailed description of data collection and the error propagation is provided in the supporting information. The individual aliquot errors are strongly influenced by the aliquot size, where smaller aliquots resulted in higher uncertainties (See supporting information). If isotopic measurements were within uncertainty of background, they are reported as 'below detection limits', which is the case for most Th and Sm measurements.

3. Results

ESEM-EDS semi-quantitative compositional analyses on magnetite grains and fragments confirm that all samples contain Fe and O concentrations consistent with magnetite and/or hematite (65–75% Fe, 25–35% O), but not goethite or other Fe oxy-hydroxides. Note that samples used for dating were magnetic (attracted to hand magnet), consistent with magnetite. No other major cations were detected above the 1 wt.% detection limit, with the exception of one magnetite sample (15OM21) taken from the red-green zoned upper outcrop near the unconformity, which contained 1–2 wt.% Si (aliquots noted in Table 1).

3.1. (U-Th)/He Age Results From Upper Outcrop Near the Unconformity

Carbonate-vein magnetite from sample (15OM21) produced eight aliquots, each composed of 1–5 abraded grains, with total aliquot masses of 47 to 1850 μg and average grain masses from 24 to 1850 μg. Uranium concentrations were low, ranging from 2.6 to 25.3 ng/g. Four aliquots had Th concentrations below detection limits, and four aliquots had Th <1 to 6 ng/g. Samarium was below detection for all aliquots. Age results have minimum and maximum values of 4.9 ± 1.2 Ma to 24.9 ± 17.2 Ma (Table 1, Figure 5). The remaining aliquots fall within a range of 10–24 Ma. Seven out of eight aliquot ages have a negative trend with U concentration, such that the oldest ages (20–24 Ma) have the lowest concentrations, with the exception of 15OM21ab-7, which had the highest U concentration (25.3 ng/g) and the oldest age. This was the only magnetite sample to have measurable Si (1–2 wt.%) by SEM-EDS.

3.2. (U-Th)/He Age Results From Lower Outcrop Away From the Unconformity

Three samples yielded inclusion and fracture free magnetite of sufficient size for dating from the lower outcrop, one consisting of multiple small (subhedral) grains (15OM25B) and two large (>mm) euhedral grains that were broken into fragments (15OM24bg, 15OM24g2) (Figure, 4, Table 1).

Magnetite was removed from vein material in sample 15OM25B to create eight aliquots, each composed of 1–8 abraded grains, with total aliquot masses from 101 to 793 μg and average magnetite grain masses from 13 to 793 μg per aliquot. Uranium concentrations in these magnetite range from 19.9 to 64.4 ng/g, whereas Th and Sm concentrations were below detection limit for five out of the eight aliquots. Final calculated ages range from 10.5 ± 1.7 Ma to 32.7 ± 8.0 Ma, and have a negative trend with U concentration (Figure 5).

Sample 15OM24bg was a single cm-sized euhedral magnetite crystal plucked from the center of a calcite vein. Five aliquots composed of 1 to 4 internal fragments that ranged in total aliquot mass from 126 to 2028 μg, with average fragment masses of 31 to 2028 μg. The youngest and oldest aliquot results are 4.4 ± 0.6 Ma and 30.3 ± 3.2 Ma, respectively, while the three other aliquots are much more tightly constrained between ~8–11 Ma (Table 1, Figure 5). One aliquot, which produced a 4.4 ± 0.6 Ma age, exhibits anomalously high U, Th, and Sm concentrations (119, 88, and 60 ng/g, respectively), inconsistent with other aliquots from the sample (<40 ng/g). This may point to excess U and Th introduced through contamination for this analysis or may be due to internal sample heterogeneity. Similar to 15OM21 and 15OM25B, a negative age-U trend is present in this sample.

Sample 15OM24g2 also derived from a large (~5 mm) crystal within a calcite vein. Four aliquots were composed of 1 or 2 internal fragments that ranged in total aliquot mass from 126 to 665 μg and average fragment masses from 63 to 665 μg per aliquot. Results yield broadly consistent ages from 14.6 ± 1.8 Ma to 16.9 ± 1.3 Ma, mean sample age 15.7 ± 0.9 Ma (Table 1, Figure 6). Uranium concentrations varied from 15–25 ng/g, while Th and Sm were in lower concentration (<5 ng/g).

3.3. Outlier Assessment

A large apparent age dispersion (ca. 4 to 30 Ma) is observed in the entire age population and across all samples, regardless of outcrop, grain size, aliquot size, or analytical procedure, that could either be geologically significant or an analytical artifact. In order to assess this phenomenon, all aliquot data were

Table 1
Magnetite (U-Th)/He Data

Sample	Age	Error	%	U (ng/g)	err (ng/g)	Th (ng/g)	err (ng/g)	Sm (ng/g)	err (ng/g)	He (nmol/g)	err (nmol/g)	EDS spectra composition	# of grains or fragments	Mass of aliquot	Avg. mass/grain or fragment (μg)
Upper outcrop															
mg15OM21ab-1	10.2	4.0	39	14.2	1.4	3.8	3.2	b.d.l.	-	0.00085	0.00006	FeO	5	144	29
mg15OM21ab-2	10.1	3.3	32	8.5	0.7	3.3	1.6	b.d.l.	-	0.00051	0.00003	FeSiO	3	288	96
mg15OM21ab-3	13.7	4.9	36	6.0	0.5	b.d.l.	-	b.d.l.	-	0.00045	0.00003	FeSiO	1	366	366
mg15OM21ab-4	20.3	3.4	17	2.6	0.1	0.5	0.2	b.d.l.	-	0.00030	0.00001	FeSiO	1	1850	1850
mg15OM21ab-7*^	24.9	17.2	69	25.3	3.8	b.d.l.	-	b.d.l.	-	0.00375	0.00026	FeSiO	2	47	24
*mg15OM21ab-8**	*4.9*	*1.2*	*24*	17.8	*1.2*	*5.8*	*2.1*	*b.d.l.*	-	*0.00052*	*0.00004*	*FeSiO*	*4*	*218*	*55*
mg15OM21ab-9	24.0	9.8	41	2.9	0.6	b.d.l.	-	b.d.l.	-	0.00040	0.00003	FeSiO	1	310	310
mg15OM21ab-7corr	16.9	6.4	38	25.3	3.8	b.d.l.	-	b.d.l.	-	0.00255	0.0003	FeSiO	2	47	24
Mean age 15OM21: 15.9 ± 5.6 Ma															
Lower outcrop															
mg15OM25Bab-1	15.6	1.0	6	22.8	1.9	b.d.l.	-	1.6	1.4	0.00199	0.00008	FeO	1	793	793
mg15OM25Bab-2*^	27.7	4.0	14	21.8	1.5	b.d.l.	-	b.d.l.	-	0.00315	0.00017	FeO	1	196	196
mg15OM25Bab-3	16.3	1.8	11	25.8	1.9	b.d.l.	-	b.d.l.	-	0.00223	0.00013	FeO	3	284	95
mg15OM25Bab-4*^	28.8	4.2	15	25.5	1.1	b.d.l.	-	b.d.l.	-	0.00382	0.00021	FeO	3	162	54
mg15OM25Bab-5	10.5	1.7	16	64.4	9.1	9.9	8.2	b.d.l.	-	0.00370	0.00028	FeO	4	107	27
mg15OM25Bab-7*^	32.7	8.0	24	19.9	2.5	b.d.l.	-	b.d.l.	-	0.00327	0.00022	FeO	6	120	20
mg15OM25Bab-8	14.9	1.6	11	54.0	3.4	b.d.l.	-	b.d.l.	-	0.00429	0.00025	FeO	6	149	25
mg15OM25Bab-9	14.9	1.8	12	59.6	7.7	2.3	-	b.d.l.	-	0.00467	0.00029	FeO	8	101	13
mg15OM25Bab-2corr	16.1	3.9	24	21.8	1.5	b.d.l.	-	b.d.l.	-	0.00195	0.0002	FeO	1	196	196
mg15OM25Bab-4corr	18.5	4.0	22	25.5	1.1	b.d.l.	-	b.d.l.	-	0.00262	0.0002	FeO	3	162	54
mg15OM25Bab-7corr	18.8	7.8	41	20.1	1.4	b.d.l.	-	b.d.l.	-	0.00211	0.0002	FeO	6	120	20
Mean age 15OM25B: 15.7 ± 2.6 Ma															
mg15OM24bg-1	11.7	0.4	3	27.1	0.3	1.4	1.2	3.1	0.5	0.00174	0.00007	FeO	1	2028	2028
mg15OM24bg-2	10.7	1.3	12	37.7	1.7	19.3	7.6	6.4	2.5	0.00245	0.00014	FeO	2	324	162
mg15OM24bg-3	*4.4*	*0.6*	*13*	118.9	*4.4*	*87.7*	*20.1*	*60.1*	*6.6*	*0.00331*	*0.00026*	*FeO*	*4*	*126*	*31*
mg15OM24bg-4*^	30.3	3.2	11	20.1	1.4	b.d.l.	-	b.d.l.	-	0.00331	0.00017	FeO	3	359	120
mg15OM24bg-5	8.1	1.3	16	28.8	1.3	b.d.l.	-	3.4	2.0	0.00128	0.00010	FeO	2	400	200
mg15OM24bg-4corr	19.3	4.4	23	19.9	2.5	b.d.l.	-	b.d.l.	-	0.00207	0.0002	FeO	3	359	120
Mean age 15OM24bg: 12.4 ± 4.8 Ma															
mg15OM24g2-1	16.9	1.3	8	15.2	4.4	b.d.l.	-	2.1	1.2	0.00140	0.00007	FeO	1	665	665
mg15OM24g2-2	15.5	3.1	20	18.5	1.4	b.d.l.	-	3.3	2.0	0.00161	0.00009	FeO	1	421	421
mg15OM24g2-3	14.6	1.8	12	25.5	1.3	b.d.l.	-	b.d.l.	-	0.00203	0.00013	FeO	2	283	142
mg15OM24g2-4	15.9	4.8	30	24.2	15.2	b.d.l.	-	b.d.l.	-	0.00209	0.00020	FeO	2	126	63
Mean age 15OM24g2: 15.7 ± 0.9 Ma															

**Excluded from age calculation; ^ Aliquot with excess He; 'corr' denotes aliquot age recalculated with excess He corrected and used for the mean age.*

	Mean	stdev	n	
Age (^ only)	28.9	2.9	5	Calculated only for aliquots with excess He
Age (excl * and ^ aliquots)	14.9	3.9	17	Calculated excluding the aliquots with excess He
Age (excl *, incl excess He corr)	15.5	3.7	22	Calculated with the aliquots corrected for excess He

plotted in He (nmol/g) versus U (ng/g) space (Figure 5). In this daughter vs parent plot, the regressed slope for an array of data points is proportional to the sample age with the y-intercept constraining the 'initial' He concentration (Figure 6). The majority of aliquots (17 out of 24) form an isochron with a mean age of 14.3 ± 4.0 and a y-intercept within error of zero (red circles). Five aliquots plot above this line, with higher He concentrations (yellow circles). The mean age of this group is 28.9 ± 2.9 Ma, distinct from the main population. However, a regression through these 5 points yields a y-intercept of ~0.0012 nmol/g, indicative of excess 'initial' He within these aliquots. Excess

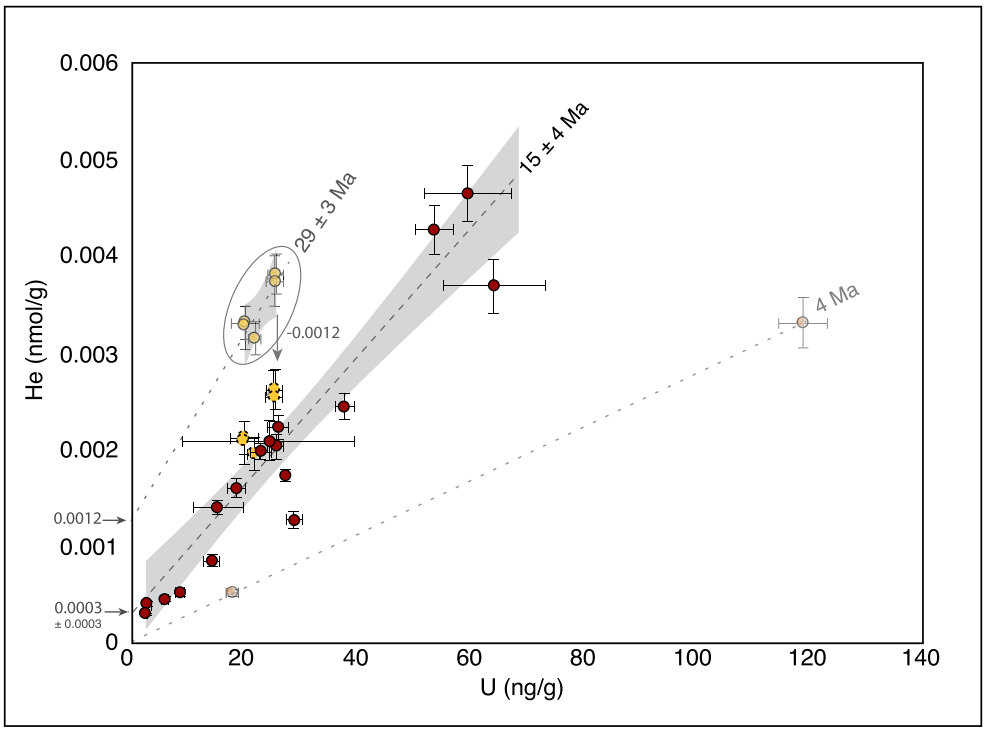

Figure 5. He (nmol/g) versus U (ng/g) for all data points. A regression line through the five oldest aliquots (solid yellow circles) has a y-intercept of 0.0012 nmol/g, indicative of excess He. Once corrected (dashed yellow circles), 22 out of 24 aliquots form a linear array with a mean age of 15.1 ± 3.9 ma with a y-intercept within error of zero.

He can be introduced by implantation from a U-Th neighbor phase or inclusion, or trapped within fluid inclusions. All grains and fragments were screened for inclusions via micro-CT, and only grains with no visible inclusions in CT data were selected for analysis. However, it is possible that an inclusion <5 μm (CT scan resolution) could contribute 'parentless' He either by He trapped in a fluid inclusion, or by a U-Th bearing mineral inclusion that ejected He into the magnetite, but was not dissolved by the magnetite dissolution procedure. Another possibility is that a ubiquitous neighboring phase (e.g., calcite) could have contributed He via implantation fairly evenly to the magnetite grains, and the 'old' grains reflect insufficient outer grain boundary removal. When corrected for excess He, by subtracting 0.0012 nmol/g, these aliquots drop to within error of the main regression and data population, and the new mean age of the population is 15.1 ± 3.9 (n = 22) with a y-intercept within error of zero.

Two out of twenty-five aliquots yielded anomalously young ages of 4–5 Ma (from 15OM24bg and 15OM21) and plot below the main population in [He] vs [U] space (Figure 5). Aliquot 15OM24bg-3, which is composed of internal fragments, is characterized by anomalously high parent isotope concentrations. We are not able to unequivocally identify the source for high U and Th in this aliquot. If the additional U and Th were supplied by a nano-inclusion within the magnetite (that was below the detection limits of the CT scan), then we would expect to see the He content contributed by this inclusion within the aliquot. Although the He concentration is slightly elevated relative to the average of the sample (Table 2), it is not significantly higher than the overall population. Alternatively, U- and Th-rich material on the magnetite grain boundary could contribute U and Th, but little He if the majority of the He is expelled outside the magnetite grain (aside from a small component implanted in the magnetite). This is possible; however, it should be noted that this magnetite was crushed and internal fragments without visible crystal faces were analyzed. A third, and perhaps most likely, possibility is contamination introduced during dissolution, which would affect the U and Th concentrations and not the He concentration. In contrast, the other 'young' aliquot (15OM21ab-8) has U, Th and He concentrations within the same range as other aliquots in the sample and so there is no obvious contamination to explain the young age. However, 4.9 Ma is outside one standard deviation of

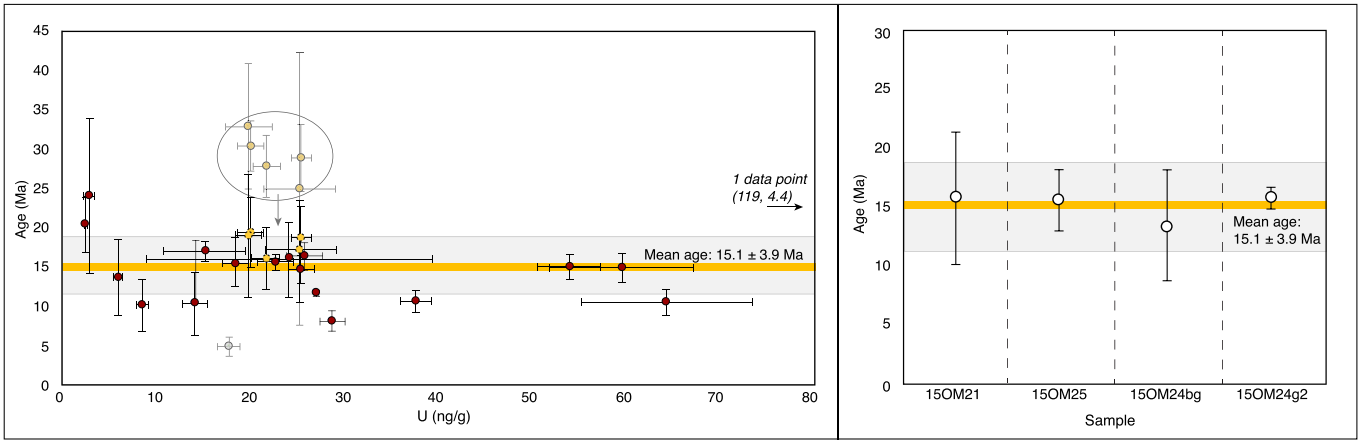

Figure 6. (left): All magnetite aliquot ages plotted against U (ng/g). Errors are propagated based on analytical uncertainties for each measurement, including the reproducibility of blanks and standards (see supporting information). Note that lower U samples have higher uncertainties. Five older aliquots (faded yellow circles) were corrected for excess He (corrected shown in dashed yellow circles). The mean age for the entire population of aliquots is 15.1 ± 3.9 Ma. (right): The mean age for individual samples are plotted with 1 stdev errors. All four samples have reproducible mean ages. Population mean age and uncertainty shown with yellow bar and gray box.

the sample mean (15.4 ± 7.7 Ma), and therefore it we treat it as an outlier. For these reasons, these two aliquots are included in all plots, but are not included in calculating the mean sample age.

Note that after filtering the individual aliquot data for outliers and He-U-Th contamination, variable and high intrasample dispersion persists (5–38%). The cause of this is not known, however, similar ranges of intrasample dispersion are observed in slowly cooled or low-U (U-Th)/He apatite data (e.g., Fitzgerald et al., 2006; McKeon et al., 2014). The concentrations of He, U, and Th in the magnetite are very low, which means that small analytical artifacts (high blanks, contamination, instrument drift) during analysis have a greater overall effect on individual aliquot results. These parameters were monitored by running procedural blanks and standards throughout each run, and the uncertainties associated with blanks and standards are propagated into the aliquot reported errors. It is observed that lower concentration aliquots have greater uncertainties, some of which are very large (for example, 15OM21 has the lowest U concentrations and the highest aliquot age uncertainties, 17–69%). Still, with the exception of 15OM24g2, the calculated uncertainties are not sufficient to explain the intrasample dispersion, pointing to other causes. Dispersion may also be caused by extended or punctuated magnetite growth over millions of years; however, we cannot resolve this within the precision of the dataset.

3.4. Sample Mean Ages

The mean ages of the individual samples are within error with the mean age calculated for the entire population of samples (Figure 6). As mentioned above, the mean age for all aliquots, including the five 'corrected' ages, is 15.1 ± 3.9 Ma (1 σ). The mean sample age for 15OM21 is 15.9 ± 5.6 Ma, for sample 15OM25 is 15.7 ± 2.6 Ma, for sample 15OM24bg is 12.4 ± 4.8 Ma, and for sample 15OM24g2 is 15.7 ± 0.9 Ma (Table 1, Figure 6). The difference in uncertainty about the mean in the individual samples reflects intra-sample dispersion of individual aliquots. Despite the variability in uncertainties, the means of each sample are consistent and all within error of each other.

4. Interpretation

4.1. Timing of Hydrothermal Magnetite Formation Within Carbonate Veins

The ability for (U-Th)/He to date the magnetite formation rather than cooling is contingent on the sample forming and remaining below the magnetite (U-Th)/He closure temperature. Given the published He diffusion kinetics for magnetite and the grain sizes of magnetite in these samples, the (U-Th)/He age should record the timing of magnetite growth for temperatures at least as high as 250 °C, potentially greater (Blackburn et al., 2007). At Wadi Fins, clumped isotope measurements on the calcite veins constrain crystallization temperatures between 25–60 °C (de Obeso & Kelemen, 2018). Given that the limestones were

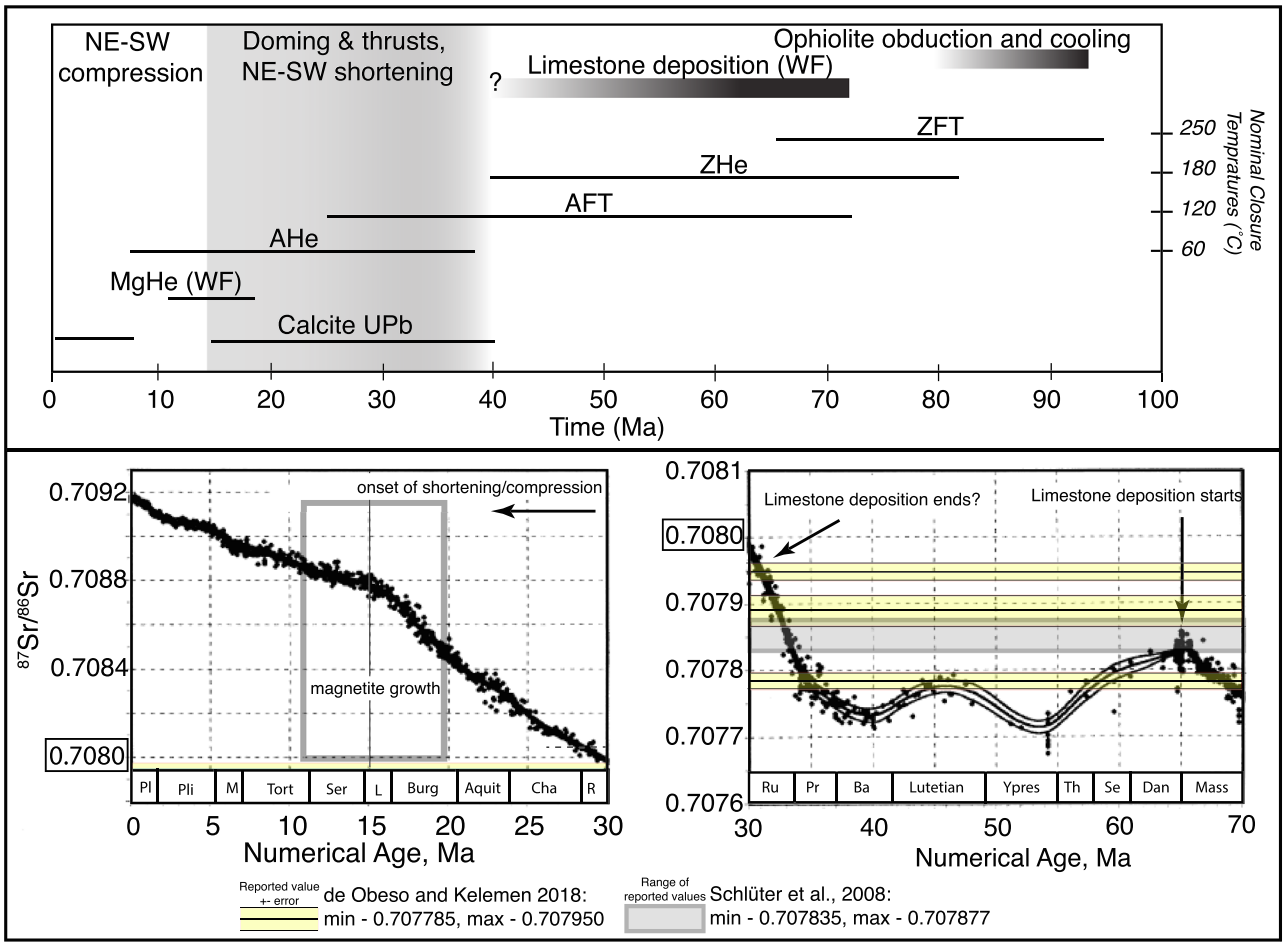

Figure 7. Top panel shows the age range of reported thermochronometric data in Oman against their respective closure temperatures (Grobe et al., 2019; Hansman et al., 2017; Poupeau et al., 1998; Saddiqi et al., 2006). Major tectonic phases relevant to the area around Wadi Fins are also noted, along with magnetite (this study) and calcite age data (Hansman et al., 2018). Bottom panel shows the Sr-isotope seawater curve (modified from Mcarthur et al., 2001) from Maastrichtian to present-day (note different scales). The gray box shows the Sr-isotope composition of the limestones at Wadi Fins (Schlüter et al., 2008). Three calcite veins from the peridotite were analyzed by de Obeso and Kelemen (2018) and are shown in yellow with their reported analytical uncertainties. Magnetite growth (this study) is indicated in the vertical gray box.

deposited in a shallow marine environment, the sedimentary overburden was limited to only 1–1.5 km, and that there is no evidence for subsequent reheating during Cenozoic tectonism and uplift based on regional thermochronology (Figure 7), we can conclude that magnetite formation occurred at temperatures well below 250 °C (likely, 25–60 °C). For these reasons, we interpret that the (U-Th)/He results represent magnetite growth rather than thermal resetting by a later event.

While individual magnetite aliquot ages range from 4.5 to 32.7 Ma, we do not regard this dispersion to be geologically meaningful or to indicate protracted magnetite formation over this entire period. As discussed above, several aliquots show evidence for the possible presence of 'initial' or 'excess' He. When corrected, these aliquots produce ages within error of the main population (Figures 5 and 6). There is also analytical evidence that at least one 4 My age is caused by contamination either in the grain or during dissolution. So, while we cannot completely rule out the possibility of multiple age generations in the magnetite, we cannot resolve magnetite growth zones within this dataset, and consider it unlikely that maximum and minimum aliquot dates reflect a period of growth. This is supported by the reproducibility of the mean sample ages, regardless of grain size, habit, or sample location which converge on a mean population age of 15.1 ± 3.9 Ma (n = 23 out 25). This is in agreement with internal fragments from the euhedral single grain 15OM24g2, the most reproducible sample, which has a mean age of 15.7 ± 0.9 Ma.

Geochemical characterization of the magnetite crystals shows that three out of four samples, regardless of grain size and habit, are chemically indistinguishable by semi-quantitative SEM-EDS. The one exception is the magnetite from the upper, more oxidized outcrop, in which magnetite grains include minor amounts of Si (1–2 w.t.%). De Obeso and Kelemen (2018) documented Si addition to the serpentinite during vein formation, and attribute the overlying limestone as the source for the Si in the alteration fluids. The detected Si in magnetite from the upper outcrop provides further evidence for Si mobility in alteration fluids, however it is not clear whether the Si mobility documented in the serpentinite and the magnetite happened at the same time or in subsequent events. Despite the presence of Si, age results in this sample are consistent with the other magnetite, suggesting that this modest chemical variation is not evidence of a separate magnetite growth episode. One interesting observation is that the Si-bearing magnetite has the lowest U concentrations.

Taken together, the overall consistency in the magnetite (U-Th)/He ages measured in each sample, regardless of analytical method, grain habit, size, and chemistry, supports the interpretation that magnetite growth occurred under similar conditions across the Wadi Fins peridotite outcrop area. Furthermore, the observation that much of the intra-sample dispersion is reproducible across all samples, and when corrected, the data converge on an average age of 15 $\pm$ 4 Ma, supports the idea that the magnetite formed during a single episode. Hence, these magnetite (U-Th)/He data appear to provide the first age constraints on hydrothermal magnetite formation in calcite veins.

For the magnetite age to constrain the timing of carbonate veining, the magnetite must be co-genetic with the veins. Magnetite occurs both as euhedral crystals in the center of veins (e.g., 15OM24bg, Figure 2f) and in trails parallel and perpendicular to the vein contact with the serpentinite (e.g., Figure 2e). The Fe to form magnetite in the calcite veins is almost certainly sourced from the serpentinite. The carbonate minerals host very little Fe (< 0.5 wt.%), whereas the serpentinite has on average 7 wt.% Fe, though some zones have up to 12% Fe (de Obeso & Kelemen, 2018, 2020). Furthermore, de Obeso and Kelemen (2018, 2020) present evidence for Si and Fe mobility in fluids that form the calcite veins and serpentinize the peridotite. For example, Fe^{2+} is fluid-mobilized during serpentinization, transported, and then deposited once it is oxidized to Fe^{3+} in upper zoned outcrop (de Obeso & Kelemen, 2020). A similar mechanism can be envisioned where fluids that interact with the serpentinite and the overlying limestone or existing calcite veins lead to calcite and magnetite deposition, including some magnetite with 1 wt.% Si.

We consider two possibilities: One interpretation is that outcrop-scale textural relationships between the magnetite crystals and calcite veins are consistent with magnetite growth concurrent with the calcite. Magnetite is present in multiple vein orientations, sizes, and crosscutting relationships in the upper and lower outcrops, which demonstrates that magnetite growth is not a localized phenomenon. Some vein magnetite contain calcite inclusions as seen in Figure 3. These and previously mentioned textural observations support that magnetite may be co-genetic with calcite and may have formed during veining. An alternative interpretation is that magnetite (re)crystallized later within already formed calcite veins, perhaps replacing a more oxidized precursor, such as hematite, as a result of diffusive interaction with the highly reducing mineral assemblages within the serpentinites (de Obeso & Kelemen 2018, 2020). If the former is true, then magnetite formation can be a proxy for the timing of carbonate veining, and would suggest that veining occurred in the Miocene. If the latter is true, then the magnetite age would record a later event that involved fluid–rock interaction and mineralization within veins that formed earlier than Miocene.

As mentioned before, the Sr-isotope composition of the limestone above the unconformity in Wadi Fins and the calcite veins in peridotite below the unconformity are consistent with Cretaceous seawater (de Obeso & Kelemen, 2018; Schlüter et al., 2008). More specifically, one of three $^{87}Sr/^{86}Sr$ values in the calcite veins overlaps within error with the limestone sequence above, a second one is consistent with Cretaceous seawater (lower value than the limestones), and a third is more radiogenic, perhaps consistent with Eocene seawater, perhaps related to leaching of radiogenic Sr from clastic material in conglomerates that are irregularly preserved along the unconformity, or perhaps from mixing of multiple sources (Figure 7). These data, in addition to field relationships, provide a plausible age for vein formation from fluids in Sr-isotope exchange equilibrium with the limestone at the Cretaceous-Tertiary boundary.

This interpretation is supported by other geologic evidence. The calcite veins are more abundant in Wadi Fins and have unique geochemical features that are not present in peridotite-hosted calcite veins

elsewhere in the Samail ophiolite. They are also found in close proximity to a Late Cretaceous unconformity. Some are flanked by oxidized alteration zones suggestive of near-surface formation. The peridotites beneath the unconformity in Wadi Fins are cut by a dense, ubiquitous network of calcite veins, whereas veins are rare in the overlying limestones. This observation is similar to that of "clastic dikes" with a micritic, limestone matrix, which extend 10 to 15 m into the peridotites beneath the unconformity, but are absent from the overlying limestones, and thus appear to root just above the unconformity. These observations are consistent with a Late Cretaceous origin for the calcite veins, but cannot easily be explained if all the veins are Miocene.

Therefore, considering all of the textural and outcrop observations described above, there are multiple possible interpretations that give weight to both the magnetite (U-Th)/He and Sr-isotope datasets. One is that that calcite veins formed in the Cretaceous, and later magnetite (re)crystallized within the veins in the Miocene. Alternatively, multiple mineralization events may be recorded in the Wadi Fins calcite veins, in the Cretaceous and Miocene, both associated with fracturing and fluid–rock interactions. Note that the calcite $^{87}Sr/^{86}Sr$ data come from the same outcrops as magnetite (U-Th)/He data, but not the same veins. Additional dating is required to test these theories.

4.2. Tectonic Influence on the Timing of Magnetite (Re)Crystallization

The timing of magnetite formation corresponds well to documented Cenozoic regional deformation and uplift (e.g., Barber et al., 2018; Hansman et al., 2017, 2018; Jacobs et al, 2015; Mouthereau et al., 2012), pointing to the influence of a tectonic driver (Figure 7). Regionally, uplift is constrained by low-temperature thermochronology. The closest low-temperature thermochronology to Wadi Fins is in the Central Oman Mountains, focused around the Jabal Akhdar and Saih Hatat structural culminations (Grobe et al., 2019; Hasman et al., 2017, Poupeau et al., 1998; Saddiqi et al., 2006) (summarized in Figure 7). While their zircon (U-Th)/He ages (Tc ~180 °C) range from Late Cretaceous to Eocene, their apatite (U-Th)/He ages (Tc ~60 °C) from the Saih Hatat and Jabal Akhdar culminations range from 26–12 Ma and 39–10 Ma, respectively (e.g., Hansman et al., 2017). Similarly, apatite (U-Th)/He on samples from outside the culminations have ages from 17–6 Ma (Hansman et al., 2017). The cooling recorded by apatite (U-Th)/He since 30 Ma appears to be linked to Oligo-Miocene surface uplift due to NE–SW shortening (Hansman et al., 2017; Hansman & Ring, 2018), and temporally coincides with the main phases of Zagros collision and rapid propagation of deformation and flexural loading of the Arabian plate (Barber et al., 2018; Mouthereau et al., 2012). The apatite (U-Th)/He ages overlap with our magnetite (U-Th)/He data from Wadi Fins.

Locally, in the Tiwi-Sur area, detailed mapping documents strike-slip and reverse faulting and folding that deform Miocene strata, which has been interpreted as evidence for Miocene compression (Founier et al., 2006; Wyns et al., 1992). Post-Miocene uplift is evidenced by the lack of any post-Late Miocene to Pliocene deposits in the Tiwi map area, and uplifted Pliocene to Pleistocene wave-cut platforms between the towns of Tiwi and Fins (Kusky et al., 2005; Mattern & Scharf, 2018; Moraetis et al., 2019; Wyns et al., 1992).

Further evidence for regional, brittle deformation in the Oman Mountains is captured by U–Pb ages on calcite fibers from brittle structures within carbonate host rocks (Hansman et al., 2018), which may record tectonic forces that affected Wadi Fins. These workers report 22 ages from 11 veins that formed within the various brittle structures. These structures are associated with 6 tectonic events, and range in age from 84 ± 5 Ma to 1.6 ± 0.6 Ma (2σ errors), including five Miocene ages, one of which lies in the range of 15 ± 4 Ma inferred for magnetite crystallization in Wadi Fins (Hansman et al., 2018). Four of their samples are from Tiwi, close to Wadi Fins, from veins in Eocene limestones overlying the Late Cretaceous unconformity and altered peridotites. Their U–Pb ages, 21.5, 33.1, 33.3, 39.0 and 40.6 Ma, are interpreted as being related mainly to NE–SW shortening.

In sum, the magnetite He data from Wadi Fins falls within an extended interval of Eocene to Holocene deformation and uplift in southern Oman. If the magnetite ages are related to calcite vein formation, Miocene deformation could have caused vein (re-)opening and enhanced fluid flow to form magnetite and late calcite. This style of deformation and veining would then be a suitable analogue for ophicarbonates formed in tectonically active oceanic or continental settings where exhumed mantle peridotite is in direct contact with limestone (e.g., Bernoulli & Weissert, 1985; Clerc et al., 2014; DeFelipe et al., 2017; Surour & Arafa, 1997).

5. Conclusions

In Wadi Fins, Oman, serpentinized peridotite from the mantle section of the Samail ophiolite exhibits extensive carbonate veining below an erosional unconformity with Late Cretaceous to Paleogene limestone strata (deObeso & Kelemen, 2018, 2019). In order to determine the timing of formation of magnetite within calcite veins in the peridotite, magnetite crystals from the veins were analyzed via (U-Th)/He chronometry. The presence of magnetite within calcite veins, in some cases with calcite inclusions, suggests that Fe was scavenged during fluid–rock interaction with the serpentinite and overlying limestones and/or pre-existing calcite veins. In one sample, close to the limestone contact, Si in magnetite is also evidence for Si mobility during magnetite formation. Our results place the timing of magnetite formation to 15 ± 4 Ma. The timing of magnetite (re)crystallization falls within an extended period of regional uplift and tectonism in southern Oman, pointing to a tectonic driver for vein (re) opening and fluid rock interactions that enabled magnetite growth. These data, combined with Sr-isotope compositions from vein material, suggest the possibility of multiple fluid flow and fracturing events, in the Cretaceous and then in the Miocene, which is unique compared to other peridotite-serpentinite carbonate and veining systems in Oman. This setting may serve as an appropriate analogue for other serpentinite systems covered with thick limestone sequences in Oman and in modern seafloor environments.

Acknowledgments

This research was supported by a National Science Foundation (NSF) Graduate Research Fellowship to E.H. G. Cooperdock, the UTChron Laboratory at The University of Texas at Austin, the Chevron (Gulf) Centennial Professorship to D.F. Stockli, and by a Sloan Foundation grant awarded to P.B. Kelemen. We are grateful to Desmond Patterson for assistance and training with He measurements and data reduction, to Jessie Maisano for technical support with the X-Ray Computed Tomography. These data and images were produced at the High-Resolution X-ray Computed Tomography Facility of the University of Texas at Austin. EHGC is grateful to Jaime Barnes, Richard Ketcham, Frieder Klein and Othmar Müntener for helpful comments on an earlier version of this manuscript. Thank you to Fin Stuart and Uwe Ring for their helpful reviews, and Stephen Parman for feedback and editorial handling of the manuscript. The (U-Th)/He data in this manuscript are available in the GeoChron repository (https://www.geochron.org) and sample IGSNs are in the SESAR database (http://www.geosamples.org).

References

Al-Khirbash, S. (2015). Genesis and mineralogical classification of Ni-laterites, Oman Mountains. *Ore Geology Reviews*, *65*, 199–212. https://doi.org/10.1016/j.oregeorev.2014.09.022

Al-Khirbash, S. A. (2016). Geology, mineralogy, and geochemistry of low grade Ni-lateritic soil (Oman Mountains, Oman). *Chemie der Erde - Geochemistry*, *76*(3), 363–381. https://doi.org/10.1016/j.chemer.2016.08.002

Al-lazki, A. I., Seber, D., & Sandvol, E. (2002). A crustal transect across the Oman Mountains on the eastern margin of Arabia. *GeoArabia*, *7*(1).

Alsharon, A. S., & Nasir, S. (1996). Sedimentological and geochemical interpretation of a transgressive sequence: The late cretaceous Qahlah formation in the western Oman Mountains, United Arab Emirates. *Sedimentary Geology*, *101*, 227–242.

Barber, D. E., Stockli, D. F., Horton, B. K., & Koshnaw, R. I. (2018). Cenozoic exhumation and Foreland Basin evolution of the Zagros Orogen during the Arabia-Eurasia. *Tectonics*, *37*, 1–25. https://doi.org/10.1029/2018TC005328

Bernoulli, D., & Weissert, H. (1985). Sedimentary fabrics in Alpine ophicalcites, south Pennine Arosa zone, Switzerland. *Geology*, *13*(11), 755–758. Retrieved from. https://doi.org/10.1130/0091-7613(1985)13%3C755:SFIAOS%3E2.0.CO

Blackburn, T. J., Stockli, D. F., & Walker, J. D. (2007). Magnetite (U-Th)/he dating and its application to the geochronology of intermediate to mafic volcanic rocks. *Earth and Planetary Science Letters*, *259*(3–4), 360–371. https://doi.org/10.1016/j.epsl.2007.04.044

Chavagnac, V., Ceuleneer, G., Monnin, C., Lansac, B., Hoareau, G., & Boulart, C. (2013). Mineralogical assemblages forming at hyperalkaline warm springs hosted on ultramafic rocks: A case study of Oman and Ligurian ophiolites. *Geochemistry, Geophysics, Geosystems*, *14*, 2474–2495. https://doi.org/10.1002/ggge.20146

Chavagnac, V., Monnin, C., Ceuleneer, G., Boulart, C., & Hoareau, G. (2013). Characterization of hyperalkaline fluids produced by low-temperature serpentinization of mantle peridotites in the Oman and Ligurian ophiolites. *Geochemistry, Geophysics, Geosystems*, *14*, 2496–2522. https://doi.org/10.1002/ggge.20147

Clark, I. D., & Fontes, J.-C. (1990). Paleoclimatic reconstruction in northern Oman based on carbonates from Hyperalkaline Groundwaters. *Quaternary Research*, *33*(3), 320–336. https://doi.org/10.1016/0033-5894(90)90059-T

Clerc, C., Boulvais, P., Lagabrielle, Y., & de Saint Blanquat, M. (2014). Ophicalcites from the northern Pyrenean belt: A field, petrographic and stable isotope study. *International Journal of Earth Sciences*, *103*(1), 141–163. https://doi.org/10.1007/s00531-013-0927-z

Cooperdock, E. H. G., Ketcham, R. A., & Stockli, D. F. (2019). Resolving the effects of 2-D versus 3-D grain measurements on apatite (U–Th) he age data and reproducibility. *Geochronology*, *1*(1), 17–41. https://doi.org/10.5194/gchron-1-17-2019

Cooperdock, E. H. G., & Stockli, D. F. (2016). Unraveling alteration histories in serpentinites and associated ultramafic rocks with magnetite (U-Th)/he geochronology. *Geology*, *44*(11). https://doi.org/10.1130/G38587.1

de Obeso, J. C., & Kelemen, P. B. (2018). Fluid rock interactions on residual mantle peridotites overlain by shallow oceanic limestones: Insights from Wadi Fins, Sultanate of Oman. *Chemical Geology*, *498*, 139–149. https://doi.org/10.1016/j.chemgeo.2018.09.022

de Obeso, J. C., & Kelemen, P. B. (2020). Major element mobility during serpentinization, oxidation and weathering of mantle peridotite at low temperatures. *Philosophical Transactions of the Royal Society A*, *378*, 20180433. https://doi.org/10.1098/rsta.2018.0433

DeFelipe, I., Pedreira, D., Pulgar, J. A., Iriarte, E., & Mendia, M. (2017). Mantle exhumation and metamorphism in the Basque-Cantabrian Basin (N Spain): Stable and clumped isotope analysis in carbonates and comparison with ophicalcites in the north-Pyrenean zone (Urdach and Lherz). *Geochemistry, Geophysics, Geosystems*, *18*, 631–652. https://doi.org/10.1002/2016GC006690.Received

Dorale, J. A., Edwards, R. L., Alexander, E. C., Shen, C.-C., Richards, D. A., & Cheng, H. (2004). Uranium-series dating of Speleothems: Current techniques, limits, & applications BT - studies of cave sediments. In I. D. Sasowsky, & J. Mylroie (Eds.), (pp. 177–197). Boston, MA: Springer US.

Edwards, R. L., Gallup, C. D., & Cheng, H. (2003). Uranium-series dating of marine and lacustrine carbonates. *Reviews in Mineralogy and Geochemistry*, *52*(1), 363–405. Retrieved from. https://doi.org/10.2113/0520363

Falk, E. S., Guo, W., Paukert, A. N., Matter, J. M., Mervine, E. M., & Kelemen, P. B. (2016). Controls on the stable isotope compositions of travertine from hyperalkaline springs in Oman: Insights from clumped isotope measurements. *Geochimica et Cosmochimica Acta*, *192*, 1–28. https://doi.org/10.1016/j.gca.2016.06.026

Falk, E. S., & Kelemen, P. B. (2015). Geochemistry and petrology of listvenite in the Samail ophiolite, Sultanate of Oman: Complete carbonation of peridotite during ophiolite emplacement. *Geochimica et Cosmochimica Acta*, *160*, 70–90. https://doi.org/10.1016/j.gca.2015.03.014

Fitzgerald, P., Baldwin, S., Webb, L., & O'Sullivan, P. (2006). Interpretation of (U-Th)/he Single grain ages from slowly cooled crustal terranes: A case study from the Transantarctic Mountains of southern Victoria Land. *Chemical Geology*, *225*, 91–120. https://doi.org/10.1016/j.chemgeo.2005.09.001

Fournier, M., Lepvrier, C., Razin, P., & Jolivet, L. (2006). Late Cretaceous to Paleogene post-obduction extension and subsequent Neogene compression in the Oman Mountains. *GeoArabia*, *11*(4), 17–40.

Froitzheim, N., & Rubatto, D. (1998). Continental breakup by detachment faulting: Field evidence and geochronological constraints (Tasna nappe, Switzerland). *Terra Nova*, *10*(4), 171–176.

Goodfellow, B. W., & Kylander-Clark, A. R. C. (2017). Palaeocene Faulting in SE Sweden from U – Pb Dating of Slickenfibre Calcite Sw N Sample Site. *Terra Nova*, *29*, 321–328. https://doi.org/10.1111/ter.12280

Grobe, A., Von Hagke, C., Littke, R., Dunkl, I., Wübbeler, F., Muchez, P., & Urai, J. L. (2019). Tectono-Thermal Evolution of Oman' S Mesozoic Passive Continental Margin under the Obducting Semail Ophiolite: A Case Study of Jebel. *Solid Earth*, *10*, 149–175. https://doi.org/10.5194/se-10-149-2019

Hacker, B. R. (1994). Rapid Emplacement of Young Oceanic Lithosphere: Argon Geochronology of the Oman Ophiolite. *Science*, *265*(5178), 1563 LP–1565. https://doi.org/10.1126/science.265.5178.1563

Hansman, R. J., Albert, R., Gerdes, A., & Ring, U. (2018). Absolute ages of multiple generations of brittle structures by U-Pb dating of calcite absolute ages of multiple generations of brittle structures by U – Pb dating of calcite. *Geology*, *46*(3), 207–210. https://doi.org/10.1130/G39822.1

Hansman, R. J., & Ring, U. (2018). Jabal Hafit anticline (UAE and Oman) formed by décollement folding followed by trishear fault-propagation folding. *Journal of Structural Geology*, *117*, 168–185. https://doi.org/10.1016/j.jsg.2018.09.014

Hansman, R. J., Ring, U., Thomson, S. N., den Brok, B., & Stübner, K. (2017). Late Eocene uplift of the Al Hajar Mountains, Oman, supported by stratigraphy and low-temperature Thermochronology. *Tectonics*, *36*, 3081–3109. https://doi.org/10.1002/2017TC004672

Jacobs, J., Thomas, R. J., Ksienzyk, A. K., & Dunkl, I. (2015). Tracking the Oman Ophiolite to the surface - New fission track and (U-Th)/He data from the Aswad and Khor Fakkan Blocks, United Arab Emirates. *Tectonophysics*, *644*, 68–80. https://doi.org/10.1016/j.tecto.2014.12.018

Jagoutz, O., Macdonald, F. A., & Royden, L. (2016). Low-latitude arc–continent collision as a driver for global cooling. *Proceedings of the National Academy of Sciences*, *113*(18), 4935 LP–4940. https://doi.org/10.1073/pnas.1523667113

Jahn, B., & Cuvellier, H. (1994). Pb-Pb and U- Pb geochronology of carbonate rocks: An assessment. *Chemical Geology*, *115*, 125–151.

Kelemen, P. B., & Manning, C. E. (2015). Reevaluating carbon fluxes in subduction zones, what goes down, mostly comes up. *Proceedings of the National Academy of Sciences*. https://doi.org/10.1073/pnas.1507889112

Kelemen, P. B., & Matter, J. (2008). In situ carbonation of peridotite for CO2 storage. *Proceedings of the National Academy of Sciences*. https://doi.org/10.1073/pnas.0805794105

Kelemen, P. B., Matter, J., Streit, E. E., Rudge, J. F., Curry, W. B., & Blusztajn, J. (2011). Rates and mechanisms of mineral carbonation in Peridotite: Natural processes and recipes for enhanced, in situ CO_2 capture and storage. *Annual Review of Earth and Planetary Sciences*, *39*(1), 545–576. https://doi.org/10.1146/annurev-earth-092010-152509

Kerrick, D. M., & Connolly, J. A. D. (1998). Subduction of ophicarbonates and recycling of CO2and H2O. *Geology*, *26*(4), 375–378. https://doi.org/10.1130/0091-7613(1998)026<0375:SOOARO>2.3.CO;2

Ketcham, R. A., Gautheron, C., & Tassan-Got, L. (2011). Accounting for long alpha-particle stopping distances in (U-Th-Sm)/he geochronology: Refinement of the baseline case. *Geochimica et Cosmochimica Acta*, *75*(24), 7779–7791. https://doi.org/10.1016/j.gca.2011.10.011

Klein, F., & Garrido, C. J. (2011). Thermodynamic constraints on mineral carbonation of serpentinized peridotite. *Lithos*, *126*(3–4), 147–160. https://doi.org/10.1016/j.lithos.2011.07.020

Kusky, T., Robinson, C., & El-Baz, F. (2005). Tertiary–Quaternary faulting and uplift in the northern Oman Hajar Mountains. *Journal of the Geological Society*, *162*(5), 871 LP–888. https://doi.org/10.1144/0016-764904-122

Lacinska, A. M., & Styles, M. T. (2012). Silicified serpentinite – A residuum of a tertiary palaeo-weathering surface in the United Arab Emirates. *Geological Magazine*, *150*(3), 385–395. Retrieved from. https://doi.org/10.1017/S0016756812000325

Ludwig, K. A., Shen, C.-C., Kelley, D. S., Cheng, H., & Edwards, R. L. (2011). U–Th systematics and 230Th ages of carbonate chimneys at the lost City hydrothermal field. *Geochimica et Cosmochimica Acta*, *75*(7), 1869–1888. https://doi.org/10.1016/j.gca.2011.01.008

Mann, A., Hanna, S. S., Nolan, S. C., Mann, A., & Hanna, S. S. (1990). The post-Campanian tectonic evolution of the Central Oman Mountains: Tertiary extension of the Eastern Arabian Margin. *Geological Society, London, Special Publications*, *49*(1), 549 LP–563. https://doi.org/10.1144/GSL.SP.1992.049.01.33

Mattern, F., & Scharf, A. (2018). Postobductional extension along and within the frontal range of the eastern Oman Mountains. *Journal of Asian Earth Sciences*, *154*, 369–385. https://doi.org/10.1016/j.jseaes.2017.12.031

Mcarthur, J. M., Howarth, R. J., & Bailey, T. R. (2001). Strontium Isotope Stratigraphy: LOWESS Version 3: Best Fit to the Marine Sr-Isotope Curve for 0–509 Ma and Accompanying Look-up Table for Deriving Numerical Age. *The Journal of Geology*, *109*(2), 155–170.

McKeon, R. E., Zeitler, P. K., Pazzaglia, F. J., Idleman, B. D., & Enkelmann, E. (2014). Decay of an old orogen: Inferences about Appalachian landscape evolution from low-temperature thermochronology. *GSA Bulletin*, *126*(1–2), 31–46. https://doi.org/10.1130/B30808.1

Mervine, E. M., Humphris, S. E., Sims, K. W. W., Kelemen, P. B., & Jenkins, W. J. (2014). Carbonation rates of peridotite in the Samail Ophiolite, Sultanate of Oman, constrained through 14 C dating and stable isotopes. *Geochimica et Cosmochimica Acta*, *126*, 371–397. https://doi.org/10.1016/j.gca.2013.11.007

Mervine, E. M., Sims, K. W. W., Humphris, S. E., & Kelemen, P. B. (2015). Applications and limitations of U – Th disequilibria systematics for determining ages of carbonate alteration minerals in peridotite. *Chemical Geology*, *412*, 151–166. https://doi.org/10.1016/j.chemgeo.2015.07.023

Miller, H. M., Matter, M., Kelemen, P., Ellison, E. T., Conrad, M. E., Fierer, N., et al. (2016). Modern water/rock reactions in Oman hyperalkaline peridotite aquifers and implications for microbial habitability. *Geochimica et Cosmochimica Acta*, *179*, 217–241. https://doi.org/10.1016/j.gca.2016.01.033

Moraetis, D., Mattern, F., Scharf, A., Frijia, G., Kusky, T. M., Yuan, Y., & El-hussain, I. (2019). Neogene to Quaternary Uplift History along the Passive Margin of the Northeastern Arabian Peninsula, Eastern Al Hajar Mountains, Oman. *Quaternary Research*, *90*(2), 418–434. https://doi.org/10.1017/qua.2018.51

Mouthereau, F., Lacombe, O., & Vergés, J. (2012). Building the Zagros collisional orogen: Timing, strain distribution and the dynamics of Arabia/Eurasia plate convergence. *Tectonophysics*, *532–535*, 27–60. https://doi.org/10.1016/j.tecto.2012.01.022

Nadoll, P., Angerer, T., Mauk, J. L., French, D., & Walshe, J. (2014). The chemistry of hydrothermal magnetite: A review. *Ore Geology Reviews*, *61*, 1–32. https://doi.org/10.1016/j.oregeorev.2013.12.013

Nasir, S., Al Sayigh, A. R., Al Harthy, A., Al-Khirbash, S., Al-Jaaidi, O., Musllam, A., et al. (2007). Mineralogical and geochemical characterization of listwaenite from the Semail Ophiolite, Oman. *Chemie der Erde - Geochemistry*, *67*(3), 213–228. https://doi.org/10.1016/j.chemer.2005.01.003

Neal, C., & Stanger, G. (1983). Hydrogen generation from mantle source rocks in Oman. *Earth and Planetary Science Letters*, *66*, 315–320.

Neal, C., & Stanger, G. (1984). Calcium and magnesium hydroxide precipitation from alkaline groundwaters in Oman, and their significance to the process of serpentinization. *Mineralogical Magazine*, *48*(June), 273–241.

Neal, C., & Stanger, G. (1985). In J. I. Dreyer (Ed.), *Past And Present Serpentinisation of Ultramafic Rocks; An Example from the Semail Ophiolite Nappe of Northern Oman* (Vol. 149). Dordrecht: Springer.

Nolan, S. C., Skelton, P. W., Clissold, B. P., & Smewing, J. D. (1990). Maastrichtian to early Tertiary stratigraphy and palaeogeography of the Central and Northern Oman Mountains. *Geological Society, London, Special Publications*, *49*(1), 495 LP–519. https://doi.org/10.1144/GSL.SP.1992.049.01.31

O'Neil, J. R., & Barnes, I. (1971). C13 and O18 compositions in some fresh-water carbonates associated with ultramafic rocks and serpentinites: Western United States. *Geochimica et Cosmochimica Acta*, *35*, 687–697. https://doi.org/10.1016/0016-7037(71)90067-6

Paukert, A. N., Matter, J. M., Kelemen, P. B., Shock, E. L., & Havig, J. R. (2012). Reaction path modeling of enhanced in situ CO2mineralization for carbon sequestration in the peridotite of the Samail Ophiolite, Sultanate of Oman. *Chemical Geology*, *330–331*, 86–100. https://doi.org/10.1016/j.chemgeo.2012.08.013

Pisapia, C., Deschamps, P., Battani, A., Buschaert, S., Guihou, A., Hamelin, B., & Brulhet, J. (2017). U/Pb dating of geodic calcite: New insights on Western Europe major tectonic events and associated diagenetic fluids. *Journal of the Geological Society*, *175*(1), 60–70. https://doi.org/10.1144/jgs2017-067

Poupeau, G., Cnrs, U., Fourier, U. J., Gignoux, M., Saddiqi, O., Goffé, B., & Oberhänsli, R. (1998). Late Thermal Evolution of the Oman Mountains Subophiolitic Windows: Apatite Fission-Track Thermochronology. *Geology*, *12*, 1139–1142.

Reusch, D. N. (2011). New Caledonian Carbon Sinks at the Onset of Antarctic Glaciation. *Geology*, *39*(9), 807–810. https://doi.org/10.1130/G31981.1

Rioux, M., Bowring, S., Kelemen, P., Gordon, S., Dudás, F., & Miller, R. (2012). Rapid crustal accretion and magma assimilation in the Oman: U. A. E. ophiolite: High precision U-Pb zircon geochronology of the gabbroic crust. *Journal of Geophysical Research*, *117*, B07201. https://doi.org/10.1029/2012JB009273

Rioux, M., Bowring, S., Kelemen, P., Gordon, S., Miller, R., & Dudás, F. (2013). Tectonic development of the Samail ophiolite: High-precision U-Pb zircon geochronology and Sm-Nd isotopic constraints on crustal growth and emplacement. *Journal of Geophysical Research - Solid Earth*, *118*, 2085–2101. https://doi.org/10.1002/jgrb.50139

Roberts, N. M. W., & Walker, R. J. (2016). U-Pb geochronology of calcite-mineralized fault: Absolute timing of rift-related fault events on the northeast Atlantic margin. *Geology*, *44*, 531-534. https://doi.org/10.1130/G37868.1

Robertson, A. H. F. (1987). The transition from a passive margin to an upper cretaceous foreland basin related to ophiolite emplacement in the Oman Mountains. *GSA Bulletin*, *99*(5), 633–653. https://doi.org/10.1130/0016-7606(1987)99<633:TTFAPM>2.0.CO;2

Robertson, A. H. F., & Searle, M. P. (1990). The northern Oman Tethyan continental margin: stratigraphy, structure, concepts and controversies. *Geological Society, London, Special Publications*, *49*(1), 3 LP–25. https://doi.org/10.1144/GSL.SP.1992.049.01.02

Saddiqi, O. M. A. R., Michard, A. N., Goffe, B. R., Poupeau, G. É., & Oberhänsli, R. O. (2006). Fission-Track Thermochronology of the Oman Mountains Continental Windows, and Current Problems of Tectonic Interpretation. *Bulletin de la Société Géologique de France*, *177*, 127–134.

Scambelluri, M., Bebout, G. E., Belmonte, D., Gilio, M., Campomenosi, N., Collins, N., & Crispini, L. (2016). Carbonation of subduction-zone serpentinite (high-pressure ophicarbonate; Ligurian Western Alps) and implications for the deep carbon cycling. *Earth and Planetary Science Letters*, *441*, 155–166. https://doi.org/10.1016/j.epsl.2016.02.034

Schlüter, M., Steuber, T., Parente, M., & Mutterlose, J. (2008). Evolution of a Maastrichtian-Paleocene tropical shallow-water carbonate platform (Qalhat, NE Oman). *Facies*, *54*(4), 513–527. https://doi.org/10.1007/s10347-008-0150-8

Schroeder, T., John, B., & Frost, B. R. (2002). Geologic implications of seawater circulation through peridotite exposed at slow-spreading mid-ocean ridges. *Geology*, *30*(4), 367–370. https://doi.org/10.1130/0091-7613(2002)030<0367:GIOSCT>2.0.CO;2

Schuiling, R. D., & De Boer, P. L. (2010). International journal of greenhouse gas control coastal spreading of olivine to control atmospheric CO 2 concentrations: A critical analysis of viability. Comment: Nature and laboratory models are different. *International Journal of Greenhouse Gas Control*, *4*(5), 855–856. https://doi.org/10.1016/j.ijggc.2010.04.012

Searle, M., & Cox, J. (1999). Tectonic setting, origin, and obduction of the Oman ophiolite. *Bulletin of the Geological Society of America*, *111*(1), 104–122. https://doi.org/10.1130/0016-7606(1999)111<0104:TSOAOO>2.3.CO;2

Searle, M. P., & Cox, J. (2002). Subduction zone metamorphism during formation and emplacement of the Semail ophiolite in the Oman Mountains. *Geological Magazine*, *139*(3), 241–255. Retrieved from. https://doi.org/10.1017/S0016756802006532

Skelton, P. W., Nolan, S. C., & Scott, R. W. (1990). The Maastrichtian transgression onto the northwestern flank of the Proto-Oman Mountains: sequences of rudist-bearing beach to open shelf facies. *Geological Society, London, Special Publications*, *49*(1), 521 LP–547. https://doi.org/10.1144/GSL.SP.1992.049.01.32

Smith, P. E., Farquhar, R. M., & Hancock, R. G. (1991). Direct Radiometric Age Determination of Carbonate Diagenesis Using U-Pb in Secondary Calcite. *Earth and Planetary Science Letters*, *105*, 474–491.

Stanger, G. (1985). Silicified serpentinite in the Semail nappe of Oman. *Lithos*, *18*, 13–22.

Streit, E., Kelemen, P., & Eiler, J. (2012). Coexisting serpentine and quartz from carbonate-bearing serpentinized peridotite in the Samail Ophiolite, Oman. *Contributions to Mineralogy and Petrology*, *164*(5), 821–837. https://doi.org/10.1007/s00410-012-0775-z

Surour, A. A., & Arafa, E. H. (1997). Ophicarbonates: Calichified serpentinites from Gebel Mohagara, Wadi Ghadir area, Eastern Desert, Egypt. *Journal of African Earth Sciences*, *24*(3), 315–324.

Wilde, A., Simpson, L., & Hanna, S. (2002). Preliminary study of tertiary hydrothermal alteration and platinum preliminary study of tertiary hydrothermal alteration and platinum deposition in the Oman ophiolite. *Journal of Virtual Explorer*, *6*, 7–13.

Würsten, F., Michalski, I., Le Métour, J., Mercolli, I., Matthäus, U., & Peters, T. (1991). The uplift history of the Precambrian crystalline basement of the Jabal J'alan (Sur area). In T. Peters, A. Nicolas, & R. G. Coleman (Eds.), *Ophiolite Genesis and Evolution of the Oceanic Lithosphere. Petrology and Structural Geology* (Vol. 5, pp. 613–626). Dordrecht: Springer.

Wyns, R., Bechennec, F., LeMeteour, J., & Roger, J. (1992). *Geologic Map of Tiwi. Ministry of Petroleum and Minerals*. Directorate of Minerals, Sultanate of Oman: Muscat.